Journal of Applied Geophysics 209 (2023) 104922

Contents lists available at ScienceDirect

Journal of Applied Geophysics

journal homepage: www.elsevier.com/locate/jappgeo

Application of ambient noise tomography for deep void detection

Yao Wang [a], Mohammad Khorrami [a,b], Khiem T. Tran [a,*], David Horhota [c]

[a] Department of Civil and Coastal Engineering, University of Florida, Gainesville, FL, USA
[b] Department of Geosciences, Virginia Tech, Blacksburg, VA, USA
[c] Florida Department of Transportation, Gainesville, FL, USA

ARTICLE INFO

Keywords:
Ambient noise tomography
Buried voids
Surface waves
Noninvasive testing
Cross correlation functions

ABSTRACT

This study aims to take the advantage of ambient noise recordings rich in low-frequency components for deep site characterization. We investigate the capabilities of a recently developed ambient noise tomography (ANT) method for imaging deep buried voids via both synthetic and field experiments. A challenging synthetic model with two deep voids was used to demonstrate the practicality of this ANT approach. To further test the method's capability, we conducted a field experiment at a bridge construction site in Miami, Florida, which contained a large and deep void (28 m to 44 m depth). The cross-correlation functions (CCFs) of the traffic noise recordings were directly inverted to provide subsurface S-wave velocity profiles. The results demonstrate that the method is capable of imaging deep voids. The in-situ standard penetration test (SPT) data was then compared to the inverted S-wave velocity obtained by the ANT approach. It shows that the trend of Vs and SPT values are generally in agreement, including the identification of the void and its depth. The field results suggest that the ANT is a useful geophysical tool for roadway imaging, particularly for detection of deep voids that are difficult to be imaged by active-seismic methods.

1. Introduction

Sinkholes or buried voids pose significant risks to the health of people and the safety of infrastructures such as public transportation and residential buildings. These voids need to be detected and monitored consistently, particularly in areas that are suffering from numerous sinkholes (Gutiérrez et al., 2016; Youssef et al., 2020). During the past decades, many researchers have worked on the improvement of noninvasive methods to identify and characterize voids/sinkholes (Mirzanejad et al., 2021). Detection of buried voids often begins with a noninvasive geophysical testing over a large volume of materials as it is lower costs than the invasive testing. And then, at locations with anomalies, invasive methods may be conducted to obtain detailed information of the underground media.

Seismic methods such as 2D/3D full-waveform inversion (FWI) of active-source data (Mirzanejad et al., 2020; Tran et al., 2013) have been developed for this application and showed excellent capabilities in imaging shallow voids (<15 m depth). While these methods can provide accurate subsurface profiles, they require low-frequency energy (<10 Hz) for imaging deeper voids. As large, powerful active sources capable of generating such low-frequency energy are expensive and generally not available for use on most projects, we seek to take advantage of the low-frequency ambient noise already present in the environment for deep void detection in this study.

Many ambient noise methods have been developed for subsurface site characterization. They can be categorized into three groups. The first group uses dispersion characteristics of noise fields or Green's functions (GFs), (e.g., ReMi™; Louie, 2001; Tokimatsu, 1997; Di Giulio et al., 2006; Rosenblad and Li, 2009; Endrun et al., 2010; Moschetti et al., 2010; Yang et al., 2011; Behm et al., 2016).) The dispersion curves (phase velocity versus frequency) represent the dispersion characteristics of the site, which can be inverted for 1D Vs of the subsurface. While these methods have been used successfully to develop deep 1D Vs profiles from ambient noise recordings, they average Vs over the volume of material beneath the receiver array or the receiver pair within a depth of approximately one wavelength for each frequency.

The second group uses travel time of Green's functions (GFs), which are calculated by cross-correlating long noise records between pairs of receivers located within either linear or 2D arrays. Methods using the travel time of the GFs, such as tomographic methods (Barmin et al.,

Abbreviations: ANT, ambient noise tomography; CCF, cross-correlation function; FWI, full-waveform inversion.

* Corresponding author.
E-mail address: ttk@ufl.edu (K.T. Tran).

https://doi.org/10.1016/j.jappgeo.2022.104922
Received 22 August 2022; Received in revised form 17 November 2022; Accepted 28 December 2022
Available online 30 December 2022

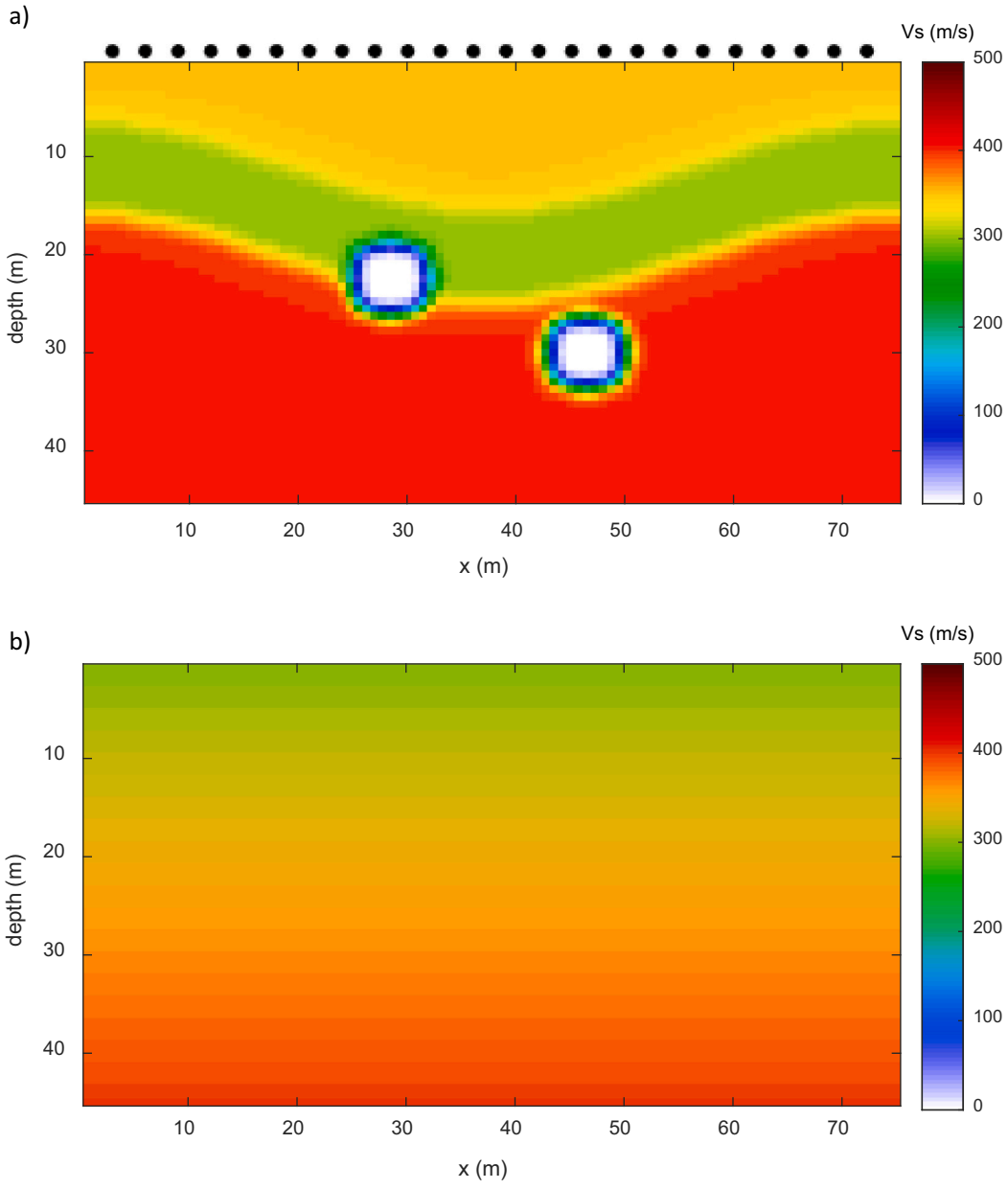

Fig. 1. The true and initial models of two-void example. a) True Vs, b) Initial Vs. The black dots in (a) denote the receiver locations.

2001) and eikonal tomography (Lin et al., 2009), have been used to obtain frequency-dependent group or phase velocity maps at regional and continental scales (e.g., Schippkus et al., 2018; Das and Rai, 2016). While these methods produce large-scale 2D velocity models, the velocities are averaged over large spatial distances.

The third group uses full-waveform inversion (FWI) of cross-correlation functions (CCF) of noise fields. Toward the FWI of CCFs, structural and source kernels were first derived by Tromp et al. (2010). The field applications have been conducted at global and local scales (De Ridder and Maddison, 2018; Sager et al., 2018). At engineering scales (tens of meters), the 2D ambient noise tomography (2D ANT; Wang et al., 2021) has recently been developed. This 2D ANT directly invert CCFs of ambient noises to extract subsurface 2D Vs profiles. The main advantage of inverting CCFs is that it does not rely on Green's function retrieval. Therefore, it doesn't require the energy balance at both sides of each receiver pair to retrieve the true GFs. The power spectrum density is estimated and included in the analysis to account for the energy source distribution. The method has been successfully used for detection of shallow voids (10 m depth) under roadway (Wang et al., 2021). In this study, we investigate the 2D ANT method's capability in detecting deep voids (>20 m depth) via both synthetic and field experiments.

2. Methodology

The 2D ANT approach (Wang et al., 2021) is used in this study. For completeness, it is briefly presented here. For the extraction of subsurface material properties, this approach involves a forward simulation of the cross-correlation function (CCF) and an adjoint-state inversion. The finite-difference solution of 2D wave equations (Tran and Hiltunen, 2012) is utilized to simulate noise and Green's functions.

2.1. Forward simulation

The CCF ($C^{\alpha\beta}$) of two signals named s^{α} and s^{β} is explicitly shown in Eq. (1):

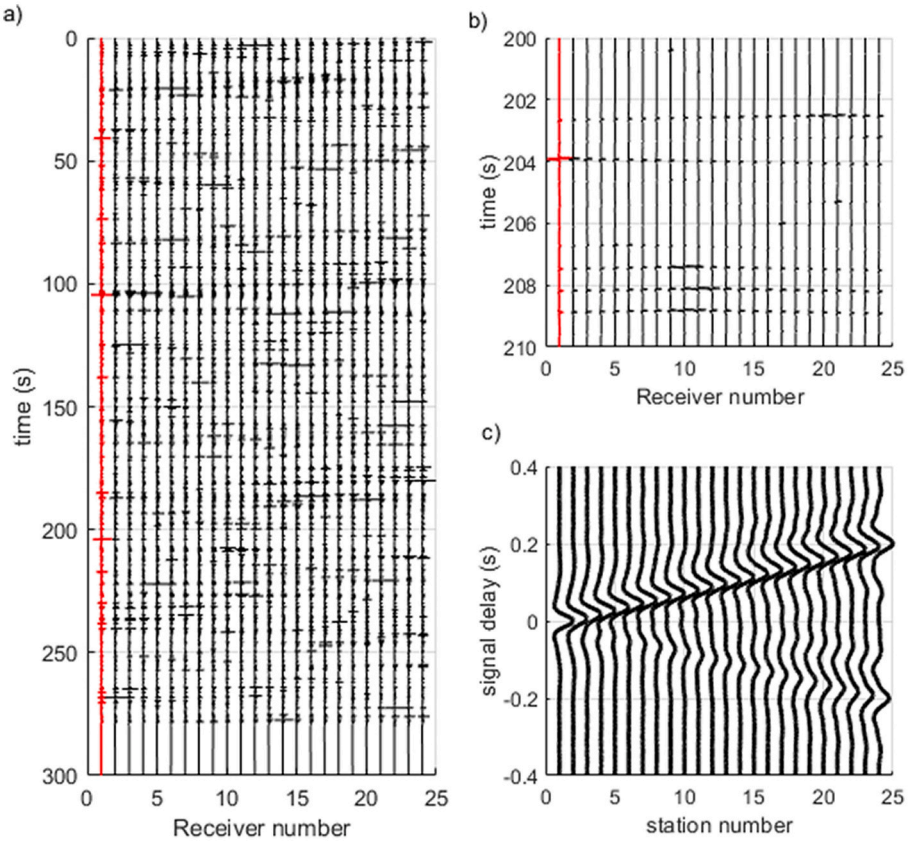

Fig. 2. Synthetic experiment: a) 5-min record of simulated traffic noise. The reference station (station #1) is highlighted with red. b) ten-second close-up of the synthetic traffic noise record. c) Cross-correlation functions at the reference station. (For interpretation of the references to colour in this figure legend, the reader is referred to the web version of this article.)

$$C^{\alpha\beta}(t) = \int s^{\alpha}(\tau)s^{\beta}(t+\tau)d\tau. \tag{1}$$

To generate seismograms $s^{\alpha}$and s^{β}, this explicit formula necessitates performing the forward simulation for every source location. Due to a large number of sources with unknown positions of noise fields, using the explicit method is not possible for inversion of the CCF. The ANT technique utilizes the implicit simulation method (Sager et al., 2018) to compute $C^{\alpha\beta}$ with a given source distribution function $S(\boldsymbol{x},\omega)$ employing reciprocity of Green's functions at receiver and source locations. The Fourier transform yields the following equivalent form of Eq. (1):

$$C^{\alpha\beta}(t) = \frac{1}{2\pi}\int s^{\alpha}(\omega)s^{\beta*}(\omega)exp(i\omega t)d\omega, \tag{2}$$

Conjugation is indicated by the asterisk. Using the Green's function, Eq. (2) can be written as:

$$C^{\alpha\beta}(t) = \frac{1}{2\pi}\int\int_{\Omega''}\int_{\Omega'} G(\boldsymbol{x}^{\alpha},\boldsymbol{x}',\omega)\,f(\boldsymbol{x}',\omega)G^{*}(\boldsymbol{x}^{\beta},\boldsymbol{x}'',\omega)\,f^{*}(\boldsymbol{x}'',\omega)exp(i\omega t)d\Omega' d\Omega'' d\omega. \tag{3}$$

where $\boldsymbol{x}'$ and $\boldsymbol{x}''$ are two spatial positions in domain Ω. The $\int_{\Omega'}d\Omega'$ and $\int_{\Omega''}d\Omega''$ express the integration twice over the space domain. The cross-correlation function $\overline{C^{\alpha\beta}(t)}$ is then averaged over a large number of realizations as:

$$\overline{C^{\alpha\beta}(t)} = \frac{1}{2\pi}\int\int_{\Omega''}\int_{\Omega'} \mathrm{G}(\boldsymbol{x}^{\alpha},\boldsymbol{x}',\omega)\mathrm{G}^{*}(\boldsymbol{x}^{\beta},\boldsymbol{x}'',\omega)\,\overline{\mathrm{f}(\boldsymbol{x}',\omega)\,\mathrm{f}^{*}(\boldsymbol{x}'',\omega)}exp(i\omega t)d\Omega' d\Omega'' d\omega. \tag{4}$$

$\overline{C^{\alpha\beta}}$ is calculated by stacking CCFs calculated over multiple time intervals (Bensen et al., 2007).

This method estimated $\overline{f(\boldsymbol{x}',\omega)\,f^{*}(\boldsymbol{x}'',\omega)}$ by assuming that the noise is

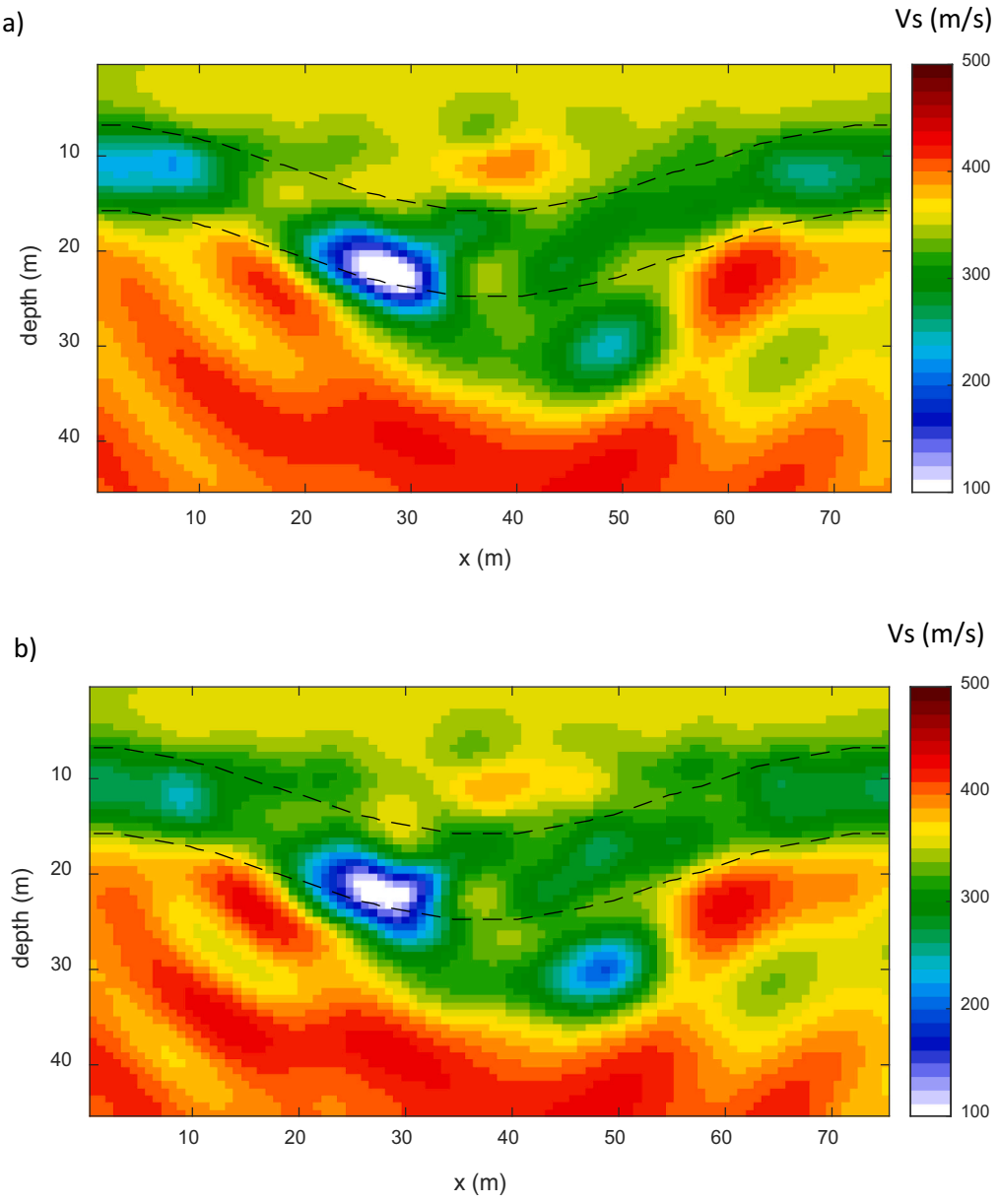

Fig. 3. Synthetic experiment: a) inverted result of the first run at 5–15 Hz and b) inverted result of the second run at 5–25 Hz.

spatially uncorrelated:

$$\overline{f(\boldsymbol{x}',\omega)f^*(\boldsymbol{x}'',\omega)} = S(\boldsymbol{x}',\omega)\delta(\boldsymbol{x}'-\boldsymbol{x}''), \tag{5}$$

with the source power-spectrum density (PSD) $S(\boldsymbol{x},\omega)$. For the noise sources that are not correlated, the CCF can be computed as:

$$\overline{C^{\alpha\beta}(t)} = \frac{1}{2\pi}\int\int_{\Omega} G(\boldsymbol{x}^{\alpha},\boldsymbol{x},\omega)G^{*}(\boldsymbol{x}^{\beta},\boldsymbol{x},\omega)\ S(\boldsymbol{x},\omega)exp(i\omega t)d\boldsymbol{x}d\omega, \tag{6}$$

The calculation of the CCF between $\boldsymbol{x}^{\alpha}$ and $\boldsymbol{x}^{\beta}$ begins with two forward simulations to compute Green's functions. The frequency-domain CCF is converted to the time domain and the PSD is calculated from the reverse-time migration of filtered CCF, as detailed in Wang et al. (2021).

2.2. Inversion

Inverting the cross-correlation function $C^{\alpha\beta}$ can obtain subsurface material properties, since the function caries the information of Green's functions with the source at $\boldsymbol{x}^{\alpha}$ and $\boldsymbol{x}^{\beta}$, as shown in Eq. (6). Taking into account the mismatch between observed and synthetic CCFs,

$$\delta C^{\alpha\beta} = C^{\alpha\beta}_{obs} - C^{\alpha\beta}_{syn} \tag{7}$$

The objective function is the L2-norm of misfit $\delta C^{\alpha\beta}$,

$$E = \frac{1}{2}\delta C^{T}\delta C = \frac{1}{2}\sum_{\alpha}\int dt\sum_{\beta}\delta C^{2} \tag{8}$$

To compute the gradient of E with respect to V_s and V_p, the adjoint-state algorithm (Tromp et al., 2010; Sager et al., 2018) is adopted in this method. For a particular location $\boldsymbol{x}^{\alpha}$, we can backward propagate the difference between the observed and synthetic CCFS from all locations $\boldsymbol{x}^{\beta}$ (Tromp et al., 2010). The modified gradient for Lamé parameters λ and μ were produced using stresses of backward-propagated cross-correlation wavefield (Shipp and Singh, 2002):

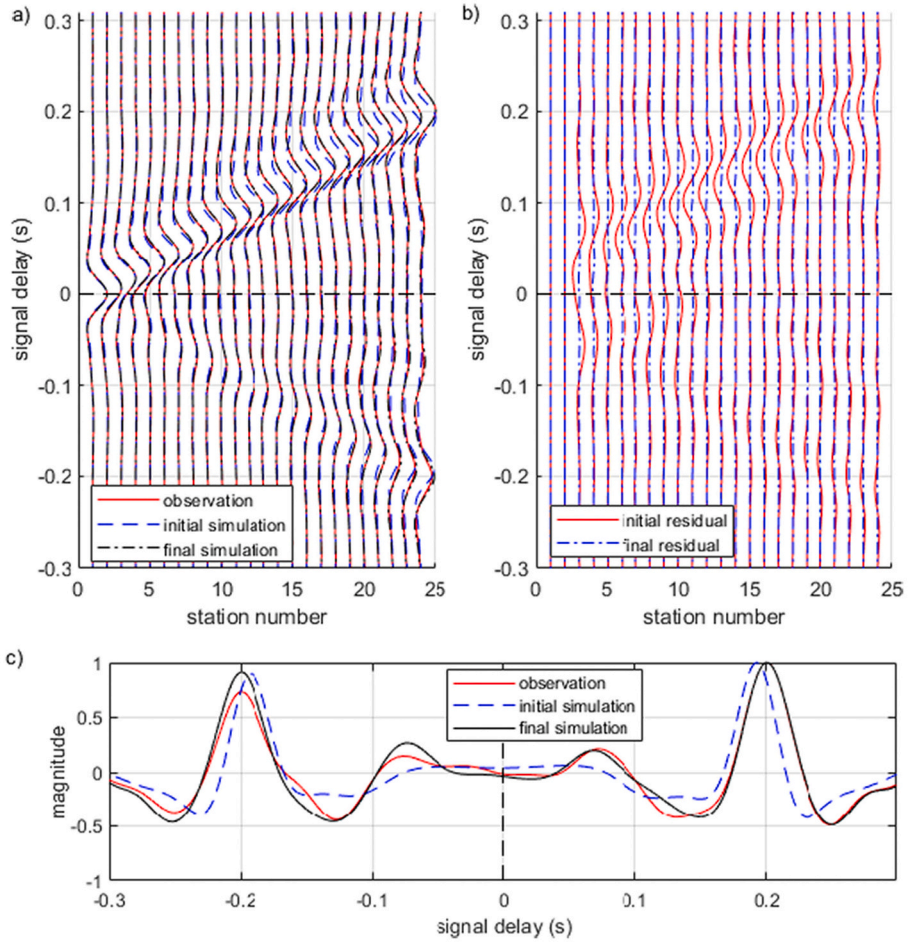

Fig. 4. Synthetic experiment: a) CCF comparison for reference station #1. b) CCF residual comparison for reference station #1. Both initial and final residuals are scaled 5 times for better visibility, c) CCF comparison at reference station #1, trace #24.

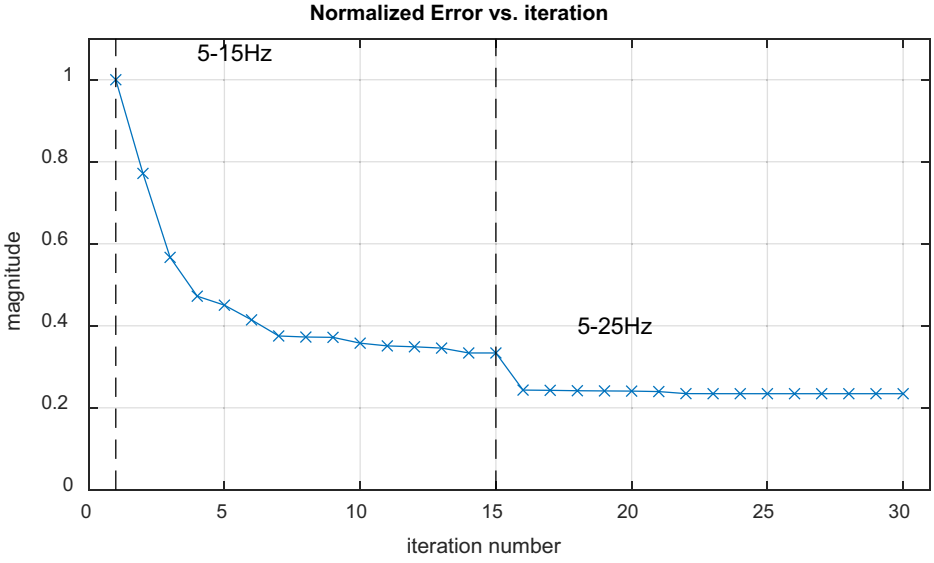

Fig. 5. Curve of normalized error versus iteration number for all two runs. Error of each iteration is normalized by dividing the initial error.

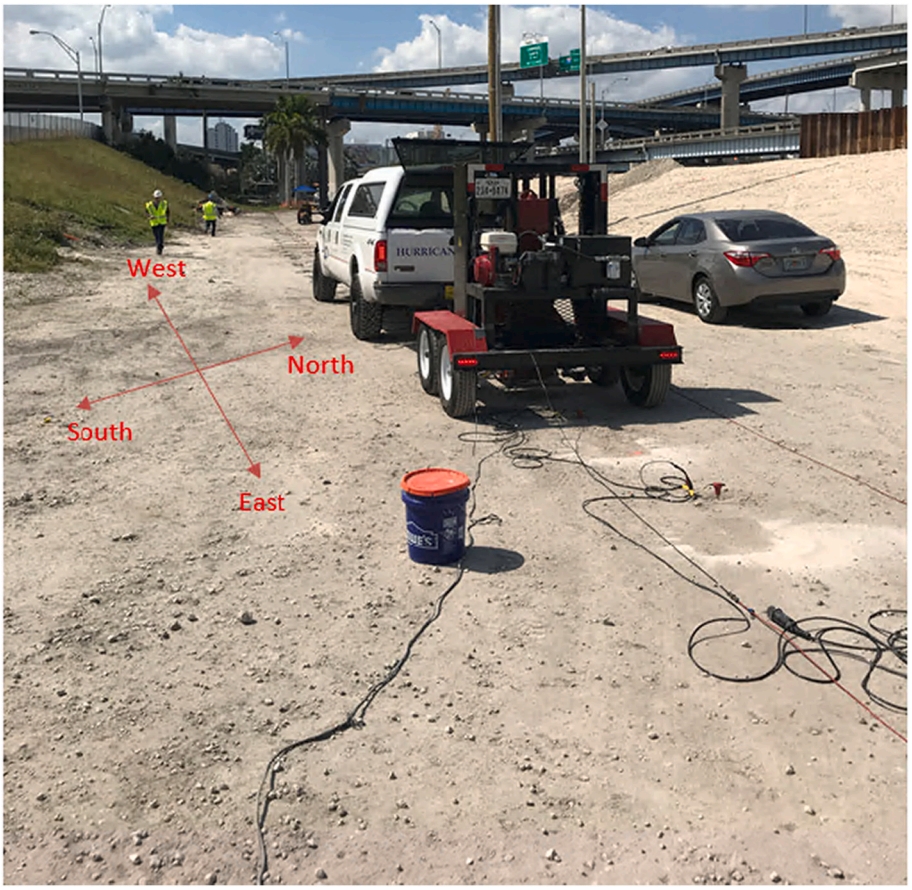

Fig. 6. Miami test site.

$$\begin{cases} \delta\lambda = -\sum_{rec}\int dt\left[\dfrac{(\sigma_{xx}+\sigma_{zz})\left[\left(\varphi_{xx}^{+}+\varphi_{zz}^{+}\right)-\left(\varphi_{xx}^{-}+\varphi_{zz}^{-}\right)\right]}{4(\lambda+\mu)^2}\right], \\ \delta\mu = -\sum_{rec}\int dt\left\{\dfrac{\sigma_{xz}\left(\varphi_{xz}^{+}-\varphi_{xz}^{-}\right)}{\mu^2}+\dfrac{1}{4}\left[\dfrac{(\sigma_{xx}+\sigma_{zz})\left[\left(\varphi_{xx}^{+}+\varphi_{zz}^{+}\right)-\left(\varphi_{xx}^{-}+\varphi_{zz}^{-}\right)\right]}{(\lambda+\mu)^2}\right.\right. \\ \left.\left.+\dfrac{(\sigma_{xx}-\sigma_{zz})\left[\left(\varphi_{xx}^{+}-\varphi_{zz}^{+}\right)-\left(\varphi_{xx}^{-}-\varphi_{zz}^{-}\right)\right]}{\mu^2}\right]\right\} \end{cases} \tag{9}$$

In Eq. (9), σ represents the stresses of forward-propagated wavefield while φ represents the stresses of backward-propagated cross-correlation wavefield. $C^{\alpha\beta}(t)$ has two lags, one positive ($t > 0$) and one negative ($t < 0$), which must be calculated independently. The stresses of the backward-propagated cross-correlation wavefield for the positive lag and the negative lag, respectively, are represented by the parameters $\varphi^{+}$and φ^{-}. The gradients can be derived as Eq. (10) considering the relationship between V_p, V_s, λ, μ, and ρ (density):

$$\begin{cases} \delta Vp = 2\rho Vp\delta\lambda, \\ \delta Vs = -4\rho Vs\delta\lambda + 2\rho Vs\delta\mu. \end{cases} \tag{10}$$

Eq. (11) gives the steepest descent direction of the *L2* misfit with respect to elastic velocities, and the model can be updated by:

$$\begin{cases} V_p^{n+1} = V_p^n + \theta_p^n \delta V_p^n, \\ V_s^{n+1} = V_s^n + \theta_s^n \delta V_s^n. \end{cases} \tag{11}$$

where in Eq. (11), step lengths θ_p and θ_s are determined utilizing a parabolic line search approach (Nocedal and Wright, 2006; Sourbier et al., 2009a, 2009b).

In first iteration, the model is updated along the steepest descent direction, and then the conjugate gradient approach is used to boost the convergence rate. The Polak-Ribière method is used to determine the search direction (Klessig and Polak, 1972). This ANT method is not capable to invert the density due to its limited sensitivity to the cross-correlation dominated by Rayleigh wave energy (Wang et al., 2021). Thus, the density is just assumed based on the available in-situ geotechnical data from the site and kept constant during the inversion process.

3. Implementation, results and discussion

In order to investigate the capabilities of the ANT method in detecting deep voids, we considered both synthetic and field experiments.

3.1. Synthetic experiment on two-void model

The synthetic model (Fig. 1a) is a realistic soil profile with variable layers and two voids of 8 m diameter embedded in deeper layers at 20 m and 30 m depths. The Vs consists of three layers of 350 m/s, 300 m/s, and 400 m/s from the top to bottom. Vp is computed from Vs using a Poisson's ratio of 0.33. Vs and Vp of voids are 0 m/s and 340 m/s (air-filled void), respectively. For wave simulation and inversion, the 75 × 45-m medium is discretized into a 100 × 60 grid of 0.75 m spacing in the x- and z-directions, respectively.

For the noise data simulation, 24 receivers at 3-m spacing are used on the free surface, shown as black dots in Fig. 1a. Synthetic traffic noise data (Fig. 2a) are simulated by the solution of 2D wave equations (Tran and Hiltunen, 2012) with multiple vehicles passing randomly in time and space in both directions (left to right and right to left). Fig. 2b is a blow-up of the synthetic data for 10 s, showing a few seismic events.

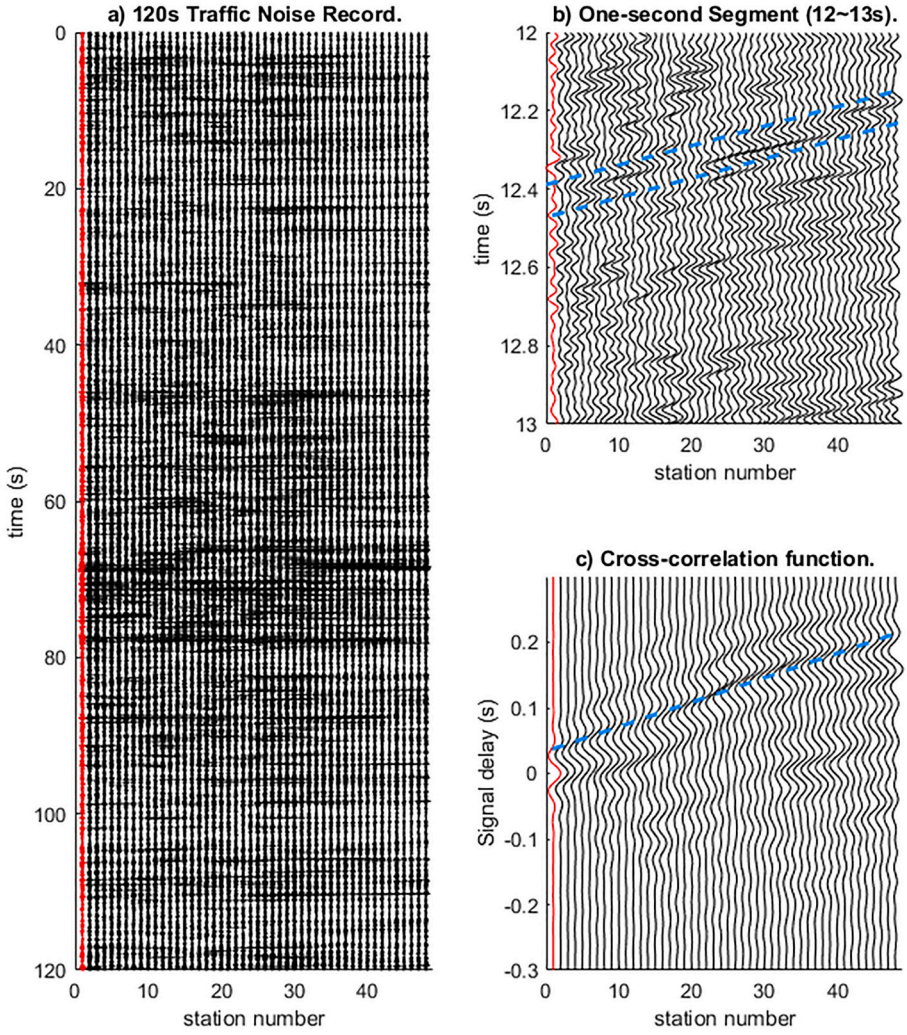

Fig. 7. Field experiment: a) Noise record after low-pass filtering (<25 Hz). b) One-second segment of the noise data. c) The retrieved CCF at the reference station (station #1). The highlighted red data is the record on the reference station. (For interpretation of the references to colour in this figure legend, the reader is referred to the web version of this article.)

CCFs are computed via Eq. (1) as shown in Fig. 2c for reference station #1. These CCFs are then assumed as those from the field data and inverted to extract the subsurface velocity structures.

For inversion, the initial Vs model is set to be laterally homogeneous. In other words, from the top to bottom, Vs increases linearly from 350 m/s to 400 m/s (Fig. 1b). The initial Vp model is twice of Vs. The inversion analysis follows the methodology described in the previous section. Both Vs and Vp are updated during the analysis as per Eq. 11. Two inversion runs were conducted with data of 5–15 Hz and 5–25 Hz, beginning at lower frequencies (5–15 Hz) on the initial model. The second run at 5–25 Hz continued on the result of the first run at 5–15 Hz. Both runs stopped after 15 iterations, for a total of 30 iterations. This multi-scale strategy (Bunks et al., 1995) helps to maintain inversion stability and avoid the cycle skipping.

Fig. 3 shows the inverted Vs profiles for both inversion runs. After the first run (Fig. 3a), the background model of the three layers is generally retrieved. Locations of the two voids are identified even with data at the low frequencies of <15 Hz. Interestingly, as the number of iterations increases, the shallow void at 20-m depth is detected earlier than the deep void at 30-m depth. Due to the spherical spreading and the decay of the wavefield, the scattered information from the shallow void is higher in magnitude and accounts for a larger contribution to the waveform misfit than the deep void. After the second run (Fig. 3b), the two voids are well imaged at the correct locations and depths. The layer interfaces are characterized, except at the region close to the two voids. This is caused by the model complexity from the scattered wavefield bouncing between the two voids. With the help of the multi-scale strategy, the inversion has successfully detected the two voids. These results demonstrate that the 2D ANT method is able to image the deep voids in complex subsurface structures.

Regarding the inverted Vp, its values only changed <10% from the initial model during inversion, the voids are not detected and thus it is not shown. While the CCFs are computed for both surface (Rayleigh) and body waves and directly inverted, the CCFs represent the similarity between pairs of channels, and thus are dominated by surface waves (propagating horizontally from one channel to another). Comparing to surface waves, reflected and refracted body waves are less correlated, and make less contribution in CCFs and inverted results. Due to the insensitivity of Rayleigh-wave dominated CCFs to Vp, it cannot be inverted with accuracy. Nevertheless, the 2D ANT method is able to image the 2 deep voids in the Vs profile.

To further assess the inversion performance, the CCF waveforms and residuals are compared in Fig. 4a and Fig. 4b, respectively. The misfit in the waveforms has been optimized and the residual is trivial after 30 iterations. A detailed waveform comparison of a single trace is shown by Fig. 4c, in which the observation and simulation are compared for the pair of receivers 1 and 24. For this pair, the two receivers are 69 m apart. The comparison evidently shows the improvement of the waveform

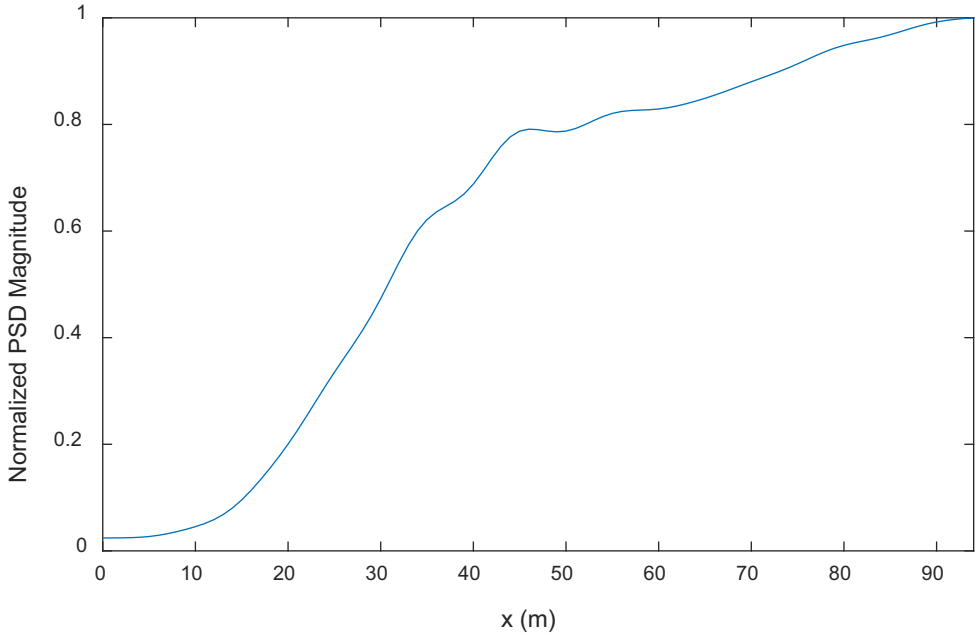

Fig. 8. Normalized estimated source power spectrum distribution (PSD) function of the field traffic noise cross-correlation function. The first station (station #1) and the last station (station #48) are located at 0 m and 94 m, respectively.

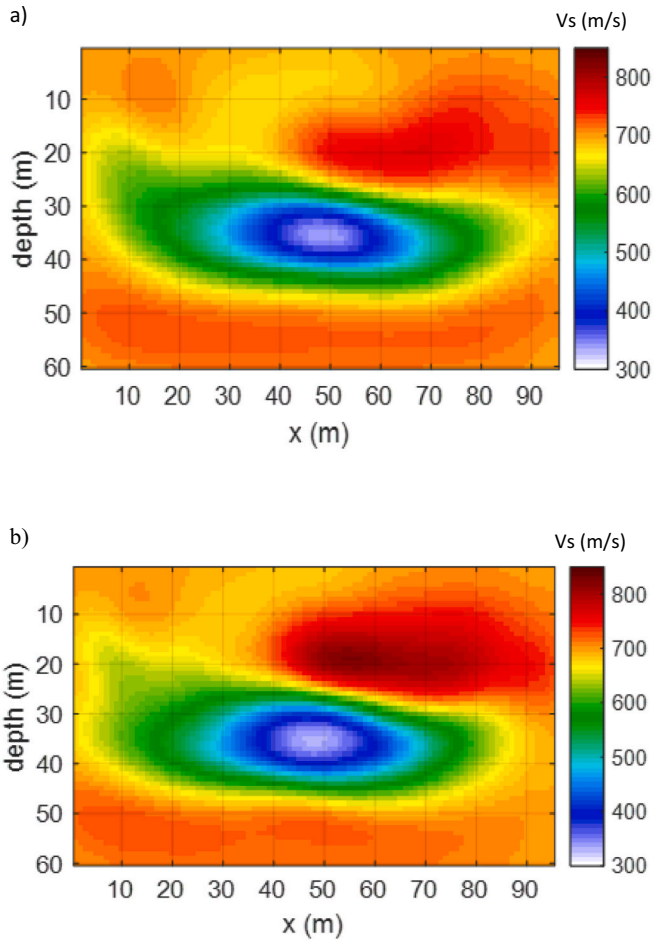

Fig. 9. Field experiment: a) Inverted Vs of the first run at 5–15 Hz. b) Inverted Vs of the second run at 5–25 Hz.

misfit during inversion. The observed and simulated data have approximately the same waveform shape and arrival time. Change of the normalized error (dividing by the initial error at the first iteration) is shown in Fig. 5. The normalized error at the final iteration (30) is approximately 22% of the initial error, indicating that the misfit in the waveform has been drastically minimized.

3.2. *Field experiment on a deep void*

To further investigate the capability of the 2D ANT method, it was applied on field experimental data. The seismic experiment was conducted at site in Miami, Florida (Fig. 6), containing a deep and large void. The site was located in an urban area, and next to Highway I-395 and many other local roads. Traffic noise data were recorded using a linear array of 48 vertical 4.5-Hz geophones at 2.0-m intervals for a spread length of 94 m. Twelve noise records were collected and each one lasted for 120 s (24 min in total). During the recording time, vehicles were frequently passing on two roadways parallel and next to the geophone line, providing good signal strength of the traffic-induced surface waves.

The seismogram of one traffic noise record is displayed in Fig. 7. The traffic noise recording is filtered to maintain low frequencies (<25 Hz) as shown in Fig. 7a. The data contain abundant traffic-induced surface waves because of the high traffic volume around the site area. A sample surface wave event (Fig. 7b) can be found at the time 12.4 s, where two blue dash lines highlight this event. The filtered data of the entire 24-min recording were then divided into 0.3 s segments, and CCFs were computed for each segment and summed over all segments. It is noted that 0.3 s was selected as it is long enough for wave propagating the entire test length of 94 m. A longer segment can be used for computing the CCFs, but it may correlate wavefields from different sources and violate the assumption of uncorrelated sources used in Eq. (6).

The sample CCFs calculated for the first reference station (receiver #1) is displayed in Fig. 7c, where the dashed line highlights the surface wave components. In the CCFs, the signals with positive lag (signal delay >0) are dominant. This means the dominant direction of in-coming surface wave signals is the direction with decreasing station numbers (from station 48 to 1). There is an evident phase shift in the surface wave

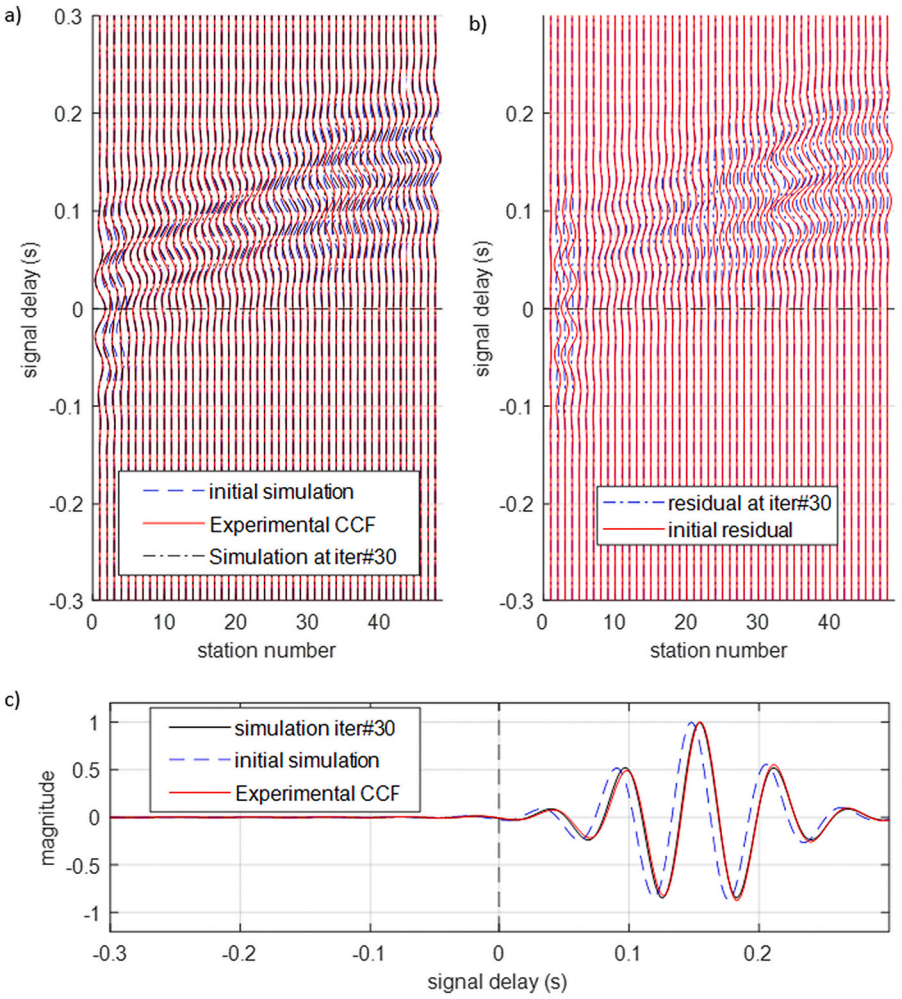

Fig. 10. a) The observed CCF, first simulation, and simulation after 30 iterations. b) Residual of the CCF. The initial residual and the residual after 30 iterations. c) Waveform comparison at reference station showing a good agreement.

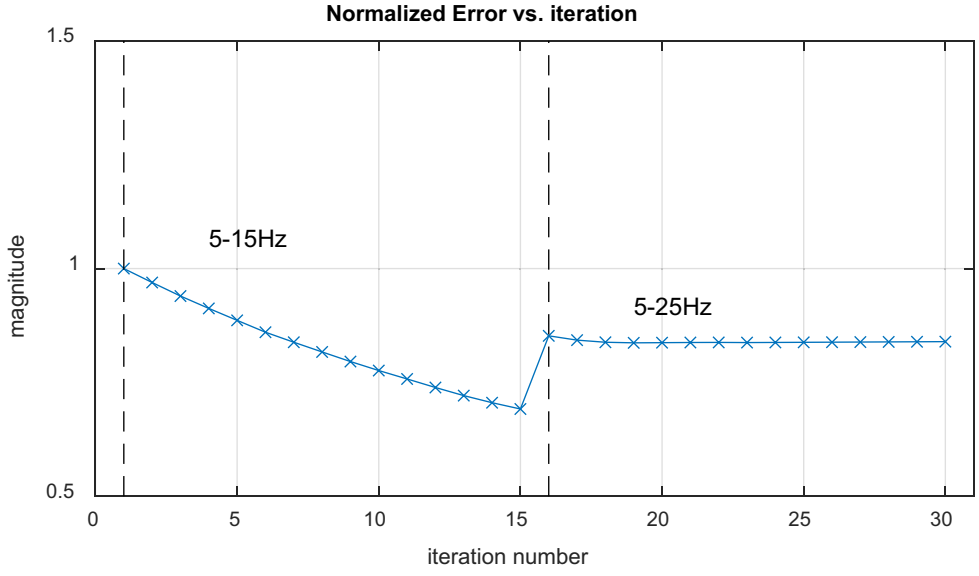

Fig. 11. Normalized misfit error vs. iteration number.

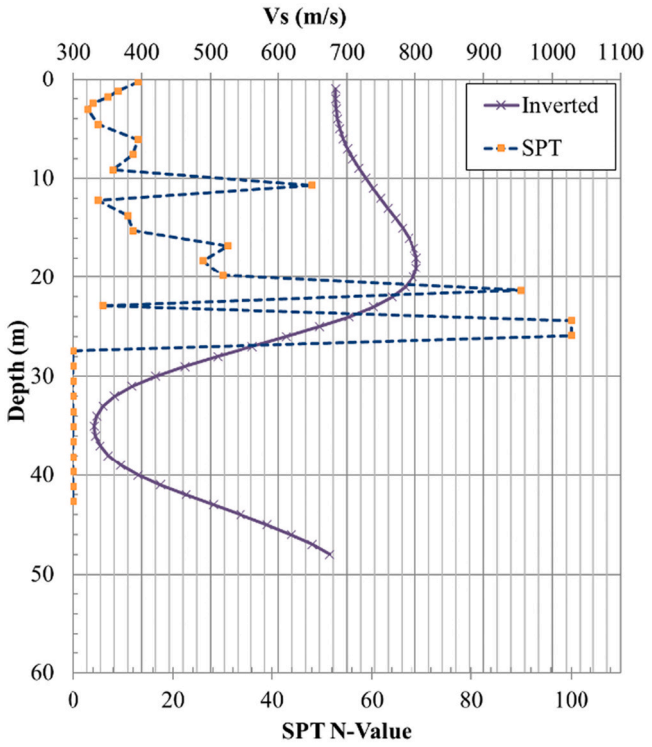

Fig. 12. Comparsion of S-wave velocity and SPT-N values at the void location.

events. The surface waves recorded by stations number 26 to 48 appear to be dragged up to the direction of positive time lag (greater time delay). This is a sign of the surface waves traveling through a low-velocity anomaly.

For this application of traffic noises, the source spatial distribution is on the road surface and next to the receiver line. We simply computed the source power spectrum density (PSD) using the reverse-time migration of the field CCF (Wang et al., 2021) at the beginning of each inversion run, and kept it constant for all iterations during each run. The computed PSD (Fig. 8) shows the source energy distribution along the test line with the largest energy at the end of the line (x = 94 m).

For inversion, the model was discretized into a 94 × 60 grid of 1 m spacing in the x- and z-directions, respectively. The grid spacing was selected as a half of the receiver spacing to conveniently assign receivers to numerical nodes. The receiver spread of 94 m was assigned on the free surface, with the first receiver at x = 0.0 m and the last receiver at x = 94 m.

The initial model was established based on the average velocity of the site. As the slope of the dashed line (Fig. 7c) is about 630 m/s (e.g., 0.15 s over a distance of 94 m), suggesting that the average Rayleigh wave velocity (V_R) of the site is about 630 m/s. As Vs is about 10% higher than V_R, a homogenous Vs model of 700 m/s was used. Vp of 1400 m/s was computed from Vs and a typical Poisson ratio of 1/3 for soil/rock, and density was assumed as 1800 kg/m^3.

The dominant frequency range of the recorded traffic noise is 5–25 Hz with consistent wave propagation pattern. Therefore, 5–25 Hz data were used for analysis. Higher frequencies (>25 Hz) are not required for deep void imaging since these short-wavelength surface wave components mostly propagate at shallow depths and do not pass by the deep void. Two inversion runs were performed with frequency bandwidths of 5–15 Hz and 5–25 Hz, respectively, beginning with the lower frequencies on the initial model. The inverted result from the first run at 5–15 Hz was used as the initial model for the second run at 5–25 Hz. Each run stopped after 15 iterations.

The inverted Vs models of both runs are displayed in Fig. 9. The first run result (Fig. 9a) shows a large low-velocity zone from about 30 m to 42 m depth, which is similar with the actual depth of the void at 28 m to 44 m. The void is successfully identified due to the low-frequency data (5–15 Hz). While the two results do not differ significantly, the second run result (Fig. 9b) shows a bit larger low-velocity zone at the void depth of 28 m to 44 m. The second run also updated the high-velocity zone above the void (consistent with the Standard Penetration Test (SPT) outputs, discussed later). Again, the void is not imaged in the inverted Vp profile, which is not shown.

The waveform comparison of the observed and simulated CCFs is shown in Fig. 10, where the red curves represent the observed CCF of traffic noise at 5–25 Hz, and the blue and black dashed curves, respectively, represent the initial and final simulated CCFs. The overall fitting of the waveforms improved during the inversion. At the large-offset stations (25 to 48) the misfit was substantially reduced. At station #48 with the largest offset from reference station #1, the optimization of surface wave arrival time is evident (Fig. 10c). Based on the time arrival, the initial simulation arrives before the observation, indicating that the starting model is stiffer than the true subsurface profile (due to the large void). After thirty iterations, the simulation and the observation have similar arrival times and match well.

The normalized misfit error is shown in Fig. 11 for all iterations. The error decreases from 1 to 0.7 in the first run and does not change much during the second run. As observed in the inverted results (Fig. 9), the first run at low-frequency data (5–15 Hz) characterized most of subsurface structure including the void. The second run mostly updated the velocity near the void boundary and the stiff rock above the void leading to a small change in the error at the second run.

For verification, Fig. 12 compares the inverted Vs and the in-situ SPT-N values. The location of both Vs and SPT is at x = 50 m, which is at the center of the void. The Vs and SPT-N profiles are generally in agreement with each other, including the identification of the void at 28–40 m depth. Albeit the lack of high frequencies has prevented the inversion algorithm from obtaining an accurate velocity profile at shallow depths, the inverted Vs is generally consistent with the trend of the SPT-N profile, which shows a high-velocity zone around 24 m depth and a low-velocity zone below 28 m. This comparison indicates that the Vs profile retrieved by the ANT method generally reflects the subsurface conditions of this site.

4. Conclusion

In this research, we investigated the capabilities of a recently developed ambient noise tomography (ANT) method for characterization of deep buried voids (sinkholes). The feasibility of the ANT method was first demonstrated on a model of variable layers with two voids of 8-m diameter, embedded at 20-m and 30-m depths. The synthetic results reveal that the 2D ANT method is capable of imaging the deep voids. Interestingly, the two voids can be identified even with data at relatively low frequencies (<15 Hz), which often exist in field traffic noises. The method was then demonstrated on a field experiment at a site in Miami, Florida, containing a deep and large void (28 m to 44 m depth). A linear array of 48 receivers were used to record traffic noises, from which CCFs were extracted and directly inverted to obtain the 2D Vs model. With the recorded traffic noise rich in low frequencies (5–15 Hz), the ANT method successfully imaged the void. The inverted Vs values generally agree with the invasive SPT-N values, including the identification of the void and its depth. Based on the field experiment, the ANT method requires less field-testing effort and reduces the risk of ground collapse due to wave excitation, comparing to active-source seismic methods. Passing vehicles of various weights and speeds can generate noise data at a wide frequency range of 5 Hz to 25 Hz required for subsurface imaging at meter-pixels to large depths (up to 50 m). Thus, the ANT method is a useful and effective geophysical tool for detecting deep voids under or near roadways.

CRediT authorship contribution statement

Yao Wang: Writing – original draft, Methodology, Data curation, Formal analysis. **Mohammad Khorrami:** Writing – original draft, Data curation, Formal analysis. **Khiem T. Tran:** Writing – review & editing, Conceptualization, Methodology, Funding acquisition, Data curation, Validation. **David Horhota:** Writing – review & editing, Methodology, Validation, Project administration.

Declaration of Competing Interest

The authors declare that they have no known competing financial interests or personal relationships that could have appeared to influence the work reported in this paper.

Data availability

Data will be made available on request.

Acknowledgements

This study was financially supported by the National Science Foundation: grant CMMI-1930697 and Florida Department of Transportation (FDOT): grant BDV31-977-122. The supports are greatly appreciated. The authors would like to thank the Universal Engineering for providing access to the test site and conducting the SPT data.

References

Barmin, M.P., Ritzwoller, M.H., Levshin, A.L., 2001. A fast and reliable method for surface wave tomography. In: Monitoring the Comprehensive Nuclear-Test-Ban Treaty: Surface Waves. Springer, pp. 1351–1375.

Behm, M., Nakata, N., Bokelmann, G., 2016. Regional ambient noise tomography in the Eastern Alps of Europe. Pure Appl. Geophys. 173, 2813–2840.

Bensen, G.D., Ritzwoller, M.H., Barmin, M.P., Levshin, A.L., Lin, F., Moschetti, M.P., Shapiro, N.M., Yang, Y., 2007. Processing seismic ambient noise data to obtain reliable broad-band surface wave dispersion measurements. Geophysical Journal International 169 (9), 1239–1260. https://doi.org/10.1111/j.1365-246X.2007.03374.x.

Bunks, C., Saleck, F.M., Zaleski, S., Chavent, G., 1995. Multiscale seismic waveform inversion. Geophysics 60 (5), 1457–1473. https://doi.org/10.1190/1.1443880.

Das, R., Rai, S.S., 2016. Seismic interferometry and ambient noise tomography: theoretical background and application in South India. J. Phys. Conf. Ser. 759, 012006.

De Ridder, S.A.L., Maddison, J.R., 2018. Full wavefield inversion of ambient seismic noise. Geophys. J. Int. 215, 1215–1230.

Di Giulio, G., Cornou, C., Ohrnberger, M., Wathelet, M., Rovelli, A., 2006. Deriving wavefield characteristics and shear-velocity profiles from two-dimensional small-aperture arrays analysis of ambient vibrations in a small-size alluvial basin, Colfiorito, Italy. Bull. Seismol. Soc. Am. 96, 1915–1933.

Endrun, B., Ohrnberger, M., Savvaidis, A., 2010. On the repeatability and consistency of three-component ambient vibration array measurements. Bull. Earthq. Eng. 8, 535–570.

Gutiérrez, F., Fabregat, I., Roqué, C., Carbonel, D., Guerrero, J., García-Hermoso, F., Zarroca, M., Linares, R., 2016. Sinkholes and caves related to evaporite dissolution in a stratigraphically and structurally complex setting, Fluvia Valley, eastern Spanish Pyrenees. Geological, geomorphological and environmental implications. Geomorphology 267, 76–97.

Klessig, R., Polak, E., 1972. Efficient implementations of the Polak–Ribière conjugate gradient algorithm. SIAM J. Control 10, 524–549.

Lin, F.-C., Ritzwoller, M.H., Snieder, R., 2009. Eikonal tomography: surface wave tomography by phase front tracking across a regional broad-band seismic array. Geophys. J. Int. 177, 1091–1110.

Louie, J.N., 2001. Faster, better: shear-wave velocity to 100 meters depth from refraction microtremor arrays. Bull. Seismol. Soc. Am. 91, 347–364.

Mirzanejad, M., Tran, K.T., McVay, M., Horhota, D., Wasman, S.J., 2020. Coupling of SPT and 3D full waveform inversion for deep site characterization. Soil Dyn. Earthq. Eng. 136, 106196.

Mirzanejad, M., Tran, K.T., McVay, M., Horhota, D., Wasman, S.J., 2021. Deep void detection with 3D full waveform inversion of surface-based and in-depth source seismic wavefields. Eng. Geol. 294, 106407.

Moschetti, M.P., Ritzwoller, M.H., Lin, F., Yang, Y., 2010. Seismic evidence for widespread western-US deep-crustal deformation caused by extension. Nature 464, 885–889.

Nocedal, J., Wright, S., 2006. Numerical Optimization. Springer Science & Business Media.

Rosenblad, B.L., Li, J., 2009. Comparative study of refraction microtremor (ReMi) and active source methods for developing low-frequency surface wave dispersion curves. J. Environ. Eng. Geophys. 14, 101–113.

Sager, K., Ermert, L., Boehm, C., Fichtner, A., 2018. Towards full waveform ambient noise inversion. Geophys. J. Int. 212, 566–590.

Schippkus, S., Zigone, D., Bokelmann, G., A. W. Group, 2018. Ambient-noise tomography of the wider Vienna Basin region. Geophys. J. Int. 215, 102–117.

Shipp, R.M., Singh, S.C., 2002. Two-dimensional full wavefield inversion of wide-aperture marine seismic streamer data. Geophys. J. Int. 151, 325–344.

Sourbier, F., Operto, S., Virieux, J., Amestoy, P., L'Excellent, J.-Y., 2009a. FWT2D: a massively parallel program for frequency-domain full-waveform tomography of wide-aperture seismic data—part 1: Algorithm. Comput. Geosci. 35, 487–495.

Sourbier, F., Operto, S., Virieux, J., Amestoy, P., L'Excellent, J.-Y., 2009b. FWT2D: a massively parallel program for frequency-domain full-waveform tomography of wide-aperture seismic data—part 2: Numerical examples and scalability analysis. Comput. Geosci. 35, 496–514.

Tokimatsu, K., 1997. Geotechnical Site Characterization Using Surface Waves: Earthquake Geotechnical Engineering.

Tran, K.T., Hiltunen, D.R., 2012. Two-dimensional inversion of full waveforms using simulated annealing. J. Geotech. Geoenviron. 138, 1075–1090.

Tran, K.T., McVay, M., Faraone, M., Horhota, D., 2013. Sinkhole detection using 2D full seismic waveform tomography. Geophysics 78, R175–R183.

Tromp, J., Luo, Y., Hanasoge, S., Peter, D., 2010. Noise cross-correlation sensitivity kernels. Geophys. J. Int. 183, 791–819.

Wang, Y., Tran, K.T., Horhota, D., 2021. Road sinkhole detection with 2D ambient noise tomography. Geophysics 86, KS123–KS135.

Yang, Y., Ritzwoller, M.H., Jones, C.H., 2011. Crustal structure determined from ambient noise tomography near the magmatic centers of the Coso region, southeastern California. Geochem. Geophys. Geosyst. 12.

Youssef, A.M., Zabramwi, Y.A., Gutiérrez, F., Bahamil, A.M., Otaibi, Z.A., Zahrani, A.J., 2020. Sinkholes induced by uncontrolled groundwater withdrawal for agriculture in arid Saudi Arabia. Integration of remote-sensing and geophysical (ERT) techniques. J. Arid Environ. 177, 104132.